JOURNAL OF COMPUTATIONAL PHYSICS **128,** 237–253 (1996)
ARTICLE NO. 0206

Improved Shock-Capturing Methods for Multicomponent and Reacting Flows

VINH T. TON[1]

Courant Institute of Mathematical Sciences, New York University, 251 Mercer Street, New York, New York 10012

Received August 15, 1995; revised May 20, 1996

Existing shock-capturing schemes have difficulties with multispecies computations, creating nonphysical glitches at species interfaces. We attribute these glitches to inconsistencies in the equation of state in cells containing several species. Our remedy is to define mixtures within a grid cell as a collection of species which can possess distinct temperatures. This formulation requires solving an additional set of species energy equations. Computational results show that the glitches have been eliminated. For chemically reacting flow simulations, existing splitting methods often generate nonphysical waves at stiff reaction fronts. We show that this numerical phenomenon is due to the mixture model that overestimates the reaction temperature. This is avoided by introducing an enforcement on the reaction temperature that depends on the temperatures of each species. We demonstrate that the method computes detonation waves with time steps and grid sizes much larger than would be allowed to resolve reaction zones.

1. INTRODUCTION

Shock-capturing methods that solve the Euler equations for single component compressible gases are well developed. However, when extending these methods to multicomponent nonequilibrium flows, a number of numerical difficulties need to be resolved. This paper addresses two open problems that have attracted considerable attention in the past several years. The first problem is the computational inaccuracies seen near contact surfaces separating thermodynamically distinct species. The second problem is the nonphysical waves generated by stiff reaction fronts. They are described in the following.

A popular approach in simulating nonreactive, multicomponent flows of compressible gases is to solve conservation laws for the mixture coupled with mass conservation equations for each species. In addition, an equation of state and an expression for the ratio of specific heats of the mixture expressed in terms of the conserved variables are given to form a closed system of equations. When typical Euler schemes are extended to solve this sytem, these methods often encounter numerical difficulties associated with contact discontinuities that separate species of different thermodynamic properties. Such problems as numerical oscillations and computational inaccuracies around contact discontinuities have been recognized and discussed in [1, 14, 17, and 25]. To circumvent the problem, Karni [14] proposes to solve the equations in terms of primitive variables. With this approach, pressure is solved directly instead of computed from the conservative variables; hence, oscillations in the pressure field can be eliminated. The drawback is that the resulting scheme is nonconservative; it can have problems in predicting shock speeds correctly. Using the high-order conservative scheme of [24], Ton *et al.* [25] show that the contact discontinuity is better resolved as the order of accuracy is increased, but the problem is not completely eliminated. Recently, Karni [15] presents a method that solves the pressure evolution equation in addition to the Euler and species conservation equations. This approach requires detection of the contact discontinuity location which is not easily accomplished for flows with three or more components or for chemically reacting flows where species are created or destroyed. Another drawback is that the method is not conservative.

In this study we show that the aforementioned errors are actually due to a thermodynamic inconsistency in the equation of state in cells containing several species; this is not a result of the numerical scheme nor numerical diffusion. The problem lies in the application of a model which assumes that all species are perfectly mixed and have the same temperature within a grid cell. This assumption is inconsistent with the possibility that contact surfaces might exist within a cell. For flows in which species can have distinct thermodynamic properties, this idealization will generate numerical spikes near contact surfaces. In this paper it is shown that, in order to eliminate this numerical artifact, each species needs to retain its own properties especially its temperature. Hence, within a cell, if mixtures are defined as a collection of species which possess distinct temperatures, contact surfaces can exist in a cell. This is sufficient to enforce thermodynamic consistency and does not require computation of the contact surface location to obtain accurate results. In order to obtain a thermodynami-

[1] Present address: The Aerospace Corporation, P.O. Box 92957, Los Angeles, CA 9009-2957.

0021-9991/96 $18.00

cally consistent model for the ratio of specific heats of the mixture, we extend the number of variables by including a set of species energy equations, in addition to the equations for species density, and for density, momentum, and energy of the mixture. Even with the added equations, a Godunov-type method will only require a Riemann problem to be solved once for the mixture of the fluid, i.e., not for each species, at each cell interface. Colella *et al.* [7] present a volume-of-fluid type method which solves a set of thermodynamically consistent equations including volume fractions and energies for each species; the scheme uses a predictor–corrector algorithm. Unlike in [7], the present approach eliminates the need to solve the evolution equations for volume fractions of each species. Implementations of the thermodynamic consistency into existing conservative, shock-capturing schemes are shown.

Modeling of reactive gas dynamics frequently is hampered by numerical difficulties arising from the stiffness of source terms representing the chemistry. It is possible to derive methods that are stable for stiff problems, but other numerical difficulties are observed. Stiffness problems can lead to stable solutions yielding nonphysical waves with incorrect wave speeds and strengths. These nonphysical phenomena have been observed numerically in [6] and [18]. Colella *et al.* [6] apply splitting methods in which the fluid dynamics and chemistry are handled in separate steps. They observe that on coarse grids the numerical solution is incorrect. In [18] both splitting methods and MacCormack-type predictor–corrector methods with flux limiters are used, and the solutions exhibit similar behavior. LeVeque and Yee [18] show that this type of difficulty is due to the nonequilibrium points at the shock front introduced by conservative shock-capturing schemes. The temperature at these points can prematurely ignite the chemical reaction. Engquist and Sjogreen [9] introduce a simple fix to this stiffness problem by preventing these nonequilibrium points from triggering the reaction. However, in this paper we will show that this difficulty is due to the *mixture* model that overestimates the reaction temperature. This stiffness problem can be eliminated with an enforcement on the reaction temperature that depends on the temperatures of each species.

In Section 2 we present various models for the ratio of specific heats of the mixture, both thermodynamically consistent and inconsistent. We illustrate the errors that result from the inconsistent models often used in practice. The set of equations to be solved numerically is derived in Section 3. Implementations of the approach into existing conservative, shock-capturing schemes are presented in Section 4. In Section 5 we present numerical results for several one- and two-dimensional problems. Comparisons with other methods are shown. High order (more than two) accurate solutions are also provided. A summary is given in the last section.

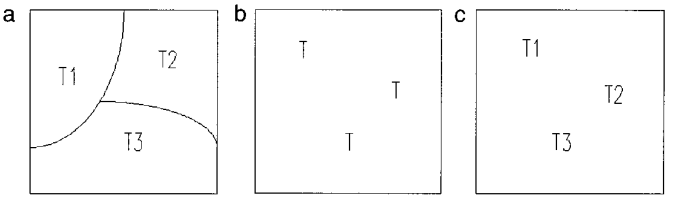

FIG. 1. Schematic of mixing models.

2. THERMODYNAMIC CONSISTENCY AND NUMERICAL SPIKES

In this section we shall analyze the numerical difficulties associated with contact discontinuities separating fluids with different thermodynamic properties. First we derive a model for the ratio of specific heats of a thermally perfect gas mixture; we deduce next a model for the ratio of specific heats of a calorically perfect gas mixture. We then show the errors resulted from using inconsistent models to simulate flows that are not in thermal equilibrium.

Consider a control volume, such as a grid cell, that is divided into subregions containing distinct species; each species can have a different temperature, as shown in Fig. 1a. The corresponding numerical representation is a mixture in which all species are perfectly mixed and have the same temperature, see Fig. 1b. It will be shown later in this section that this discrete model for the mixture will result in a thermodynamically inconsistent equation of state. Here, for numerical purposes, we define mixtures as a collection of species which possess distinct temperatures, see Fig. 1c. Each species is required to retain its own temperature. The total energy of species i per until control volume is defined as

$$\rho_i E_i = \rho_i h_i - P_i + \frac{1}{2}\rho_i \mathbf{u}\cdot\mathbf{u}, \tag{1}$$

where ρ_i, E_i, h_i, and P_i denote respectively the density of mass, total energy per unit mass, static enthalpy, and partial pressure of species i; u is the velocity of the mixture. All species are assumed to have the same velocity as the mixture. Diffusion effects are neglected in this study. The specific enthalpy of species i at temperature T_i is given by

$$h_i = h_{f,i}^0 + \int_0^{T_i} c_{p,i}\, dT \tag{2}$$

where $h_{f,i}^0$ is the specific heat of formation of species i at $T = 0$, and $c_{p,i}$ is the specific heat at constant pressure. We assume all species satisfy the ideal gas law

$$P_i = \frac{\rho_i T_i R_u}{W_i}, \tag{3}$$

where W_i represents the molecular weight of species i and R_u is the universal gas constant. Substituting the expressions for enthalpy and ideal gas law, Eq. (1) can be written as

$$\rho_i E_i = \frac{P_i}{\hat{\gamma}_i - 1} + \frac{1}{2}\rho_i \mathbf{u}\cdot\mathbf{u} + \rho_i h^0_{f,i}, \tag{4}$$

where $\hat{\gamma}_i$ is defined as

$$\hat{\gamma}_i = \frac{\hat{c}_{p,i}}{\hat{c}_{p,i} - \dfrac{R_u}{W_i}} \tag{5}$$

with

$$\hat{c}_{p,i} = \frac{1}{T_i}\int_0^{T_i} c_{p,i}\, dT. \tag{6}$$

Summing (4) over all species lead to the overall energy equation for the mixture

$$\rho E = \sum_{i=1}^{ns} \frac{P_i}{\hat{\gamma}_i - 1} + \frac{1}{2}\rho \mathbf{u}\cdot\mathbf{u} + \sum_{i=1}^{ns} \rho_i h^0_{f,i}. \tag{7}$$

Here $\rho = \sum_{i=1}^{ns} \rho_i$ represents the density of mass of the mixture, and *ns* denotes the number of species. Thus, if the total energy per unit volume for the mixture is expressed as

$$\rho E = \frac{P}{\gamma - 1} + \frac{1}{2}\rho \mathbf{u}\cdot\mathbf{u} + \sum_{i=1}^{ns} \rho_i h^0_{f,i}, \tag{8}$$

with $P = \sum_{i=1}^{ns} P_i$, then the mixture ratio of specific heats must satisfy

$$\gamma = 1 + \frac{P}{\displaystyle\sum_{i=1}^{ns} \frac{P_i}{\hat{\gamma}_i - 1}}. \tag{9}$$

For calorically perfect gas, we have $\hat{c}_{p,i} = c_{p,i}$ and $\hat{\gamma}_i = \gamma_i$.

Hence, for a thermodynamically consistent system, Eq. (9) must hold. The partial pressures, P_i, for each species are hence required to be known at each point. They cannot be computed from schemes that only provide mixture properties and species densities. The method that we shall present in the following sections is developed solely to satisfy (9). Models for γ that are widely used in practice are in fact special cases of (9) under simplifying assumptions. Two popular forms are analyzed in the following.

If all species within a grid cell are assumed to coexist at the same temperature, then Eq. (9) is reduced to a form that is used extensively in the literature, e.g. in [1, 8, 15, 16, 20, 26, 27] and many others. Substituting the ideal gas law, Eq. (9) becomes

$$\gamma = 1 + \frac{\displaystyle\sum_{i=1}^{ns} \frac{Y_i}{W_i}}{\displaystyle\sum_{i=1}^{ns} \frac{Y_i}{W_i(\gamma_i - 1)}},$$

where Y_i represents the mass fraction of species i. Introducing $\gamma_i = c_{p,i}/c_{v,i}$ leads to the equation

$$\gamma = \frac{\overline{c_p}}{\overline{c_v}} \tag{10}$$

where $\overline{c_p} = \sum_{i=1}^{ns} Y_i c_{p,i}$ and $\overline{c_v} = \sum_{i=1}^{ns} Y_i c_{v,i}$ are the mixture specific heats at constant pressure and volume, respectively. This equation for γ is valid only at a *point* in space where we can safely assume that all species coexist at the same temperature, whereas, for numerical simulation purposes, the space is divided into grid cells occupying finite volumes. The model breaks down if a contact surface separating species with different temperatures is located in the interior of a cell.

Another model for γ is introduced in [2] in an attempt to keep the pressure in equilibrium across contact discontinuities. It has the form

$$\gamma = 1 + \frac{1}{\displaystyle\sum_{i=1}^{ns} \frac{Y_i}{\gamma_i - 1}}. \tag{11}$$

It can be shown that this is a special case of (9) when the ratio of T_i/W_i is assumed constant. This implies that the model of γ in (11) guarantees the pressure will remain in equilibrium only for contact discontinuities separating species of the same densities.

The restrictions imposed by the models in (10) and (11) are impractical when simulating realistic multicomponent flows. Using these models for such flows often causes numerical spikes to be generated around contact discontinuities separating species with different thermodynamic properties. Even for flows with contact discontinuities satisfying the imposed conditions initially, passage or interaction of shocks or rarefaction waves will make both models invalid. In the following example, the generation of numerical spikes when using either (10) or (11) is illustrated. It will be shown that when a contact discontinuity separating two species of different temperature and ratio of specific heats is convected across the interior of a cell, a conservative method which only solves for mixture properties and species densities generates numerical spikes in the pressure; subsequently this will contaminate the flow field. In

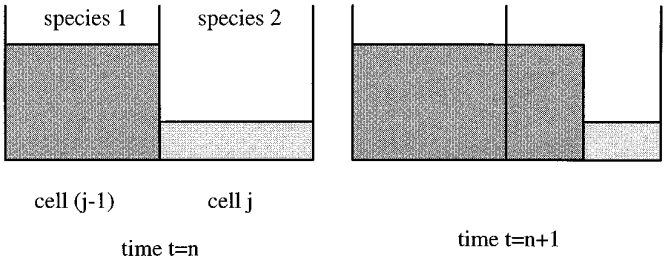

FIG. 2. Schematic of convection of a contact discontinuity.

the example, it will be also demonstrated that the source of this error is due to neither numerical diffusion nor the numerical cheme, but instead to an invalid model for the ratio of specific heats of the mixture.

EXAMPLE. Let two adjacent cells be filled with air (species 1) and helium (species 2), respectively, as shown in Fig. 2. Their properties are

$$\gamma_1 = 1.4, \qquad W_1 = 28.97\ g/mol, \qquad c_{p,1} = 1004e7\ erg/gK,$$
$$\gamma_2 = \frac{5}{3}, \qquad W_2 = 4\ g/mol, \qquad c_{p,2} = 5.196e7\ erg/gK.$$

The non-dimensional conservative values in cell $(j-1)$ are

$$\rho_1 = 1, \qquad \rho_1 E_1 = 3;$$

the corresponding values in cell j are

$$\rho_2 = .5, \qquad \rho_2 E_2 = 1.75.$$

Both cells have unit pressure and velocity. The ratio of the temperatures, T_1/T_2, is 3.621. At a later time, $t = \Delta x/2$, the contact discontinuity is convected from the cell interface to the center of cell j. Hence, the new conservative values of cell j are just the average values of cell j and $(j-1)$ from the previous time. We have

$$\rho = 0.75, \qquad \rho_1 = .5, \qquad \rho_2 = .25,$$
$$\rho E = 2.375, \qquad \rho_1 E_1 = 1.5, \qquad \rho_2 E_2 = 0.875.$$

The partial pressures can be calculated as

$$p_1 (\gamma_1 - 1)\left(\rho_1 E_1 - \frac{1}{2}\rho_1 u^2\right) = 0.5,$$

and similarly

$$p_2 = 0.5.$$

Hence, from (9), we have

$$\gamma = 1.5,$$

and pressure and velocity remain unity. Now, if either (10) or (11) is used, the value of γ are 1.583 and 1.462, respectively. The corresponding values for pressure in cell j, calculated from

$$p = (\gamma - 1)\left(\rho E - \frac{1}{2}\rho u^2\right),$$

are 1.165 and 0.923, respectively. Hence, either an overshoot or an undershoot in the pressure is generated. This type of numerical spike always occurs when an inconsistent model for γ is used along with any conservative scheme.

3. GOVERNING EQUATIONS

The standard set of governing equations for multicomponent, inviscid, compressible, reactive gas with no heat conduction consists of the Euler equations for the gas mixture and mass conservation equations for each species. The Euler equations are the conservation laws for mass, momentum, and energy. We shall express these equations in their conservative form, since this is essential in order to correctly compute (numerically) the strength and speed of discontinuities. The equations are as follows:

$$\rho_t + \nabla \cdot (\rho \mathbf{u}) = 0, \tag{12}$$
$$(\rho \mathbf{u})_t + \nabla \cdot (\rho \mathbf{u} \otimes \mathbf{u}) + \nabla P = 0, \tag{13}$$
$$(\rho E)_t + \nabla \cdot ((\rho E + P)\mathbf{u}) = 0, \tag{14}$$
$$(\rho Y_i)_t + \nabla \cdot (\rho Y_i \mathbf{u}) = \dot{\omega}_i \qquad 1 \le i \le (ns-1), \tag{15}$$

where $\dot{\omega}_i$ is the mass production/destruction rate of species i due to chemical reactions. To close the system, an equation of state, such as (8), and an algebraic expression for γ, usually (10), are given.

In order to use the consistent form of γ given in (9), additional equations are needed to determine the partial pressures for each species. The approach that we shall take is to include a set of partial differential equations written for the total energy per unit volume for each species i for $1 \le i \le (ns-1)$. Then the partial pressures for each species are calculated from (4). The remainder of this section is devoted to the derivation of the species energy equations. A similar derivation is presented in [7]. In [7], it is assumed that in a cell all species are in pressure equilibrium with one another, and all species have the same velocity as the mixture. These assumptions are also used here.

Using the continuity and momentum equations, the total

energy equation can be converted to the specific internal energy (e) equation as

$$\frac{D}{Dt}(e) - \frac{P}{\rho^2}\frac{D}{Dt}(\rho) = 0, \tag{16}$$

with

$$\frac{D}{Dt}(\,) = \frac{\partial(\,)}{\partial t} + \mathbf{u}\cdot\nabla(\,)$$

representing the material derivative. Let f_i denote the volume fraction of species i. By replacing P with P_i/f_i and ρ with ρ_i/f_i, then the corresponding equation describing the specific internal energy for species i is

$$\frac{D}{Dt}(e_i) - \frac{P_i f_i}{\rho_i^2}\frac{D}{Dt}\left(\frac{\rho_i}{f_i}\right) = 0. \tag{17}$$

Substituting the momentum and species conservation equations, the following equation is obtained:

$$\frac{\partial(\rho_i E_i)}{\partial t} + \nabla\cdot(\rho_i E_i \mathbf{u}) + Y_i \mathbf{u}\cdot\nabla P + P_i \nabla\cdot\mathbf{u} + \frac{P_i}{f_i}\frac{D}{Dt}(f_i) = 0. \tag{18}$$

Unlike [7], we want to eliminate the dependent variable f_i from the above equation. Thus, we seek an expression for $(1/f_i)(D/Dt)(f_i)$. From the definition of internal energy, $e_i = h_i - P_i/\rho_i$, we also have

$$\frac{D}{Dt}(e_i) = \frac{D}{Dt}(h_i) - \frac{1}{\rho_i}\frac{D}{Dt}(P_i) + \frac{P_i}{\rho_i^2}\frac{D}{Dt}(\rho_i). \tag{19}$$

If each species satisfies the ideal gas law, then we have

$$\frac{D}{Dt}(h_i) = c_{p,i}\frac{D}{Dt}(T_i) \tag{20}$$

with $c_{p,i}$ depending only on temperature. Substituting the above equation and the ideal gas law into (19), we have

$$\frac{D}{Dt}(e_i) = \frac{1}{(\gamma_i - 1)\rho_i}\frac{D}{Dt}(P_i) - \frac{P_i}{(\gamma_i - 1)\rho_i^2}\frac{D}{Dt}(\rho_i). \tag{21}$$

Combining the above equation with (17), and also using the species conservation equation, we obtain

$$\frac{1}{f_i}\frac{D}{Dt}(f_i) + \frac{1}{(\gamma_i - 1)P_i}\frac{D}{Dt}(P_i) + \frac{\gamma_i}{(\gamma_i - 1)}\nabla\cdot\mathbf{u} = 0. \tag{22}$$

In deriving the conservation laws, it is presumed that all species coexist independently, each obeying the laws of dynamics and thermodynamics. Hence, each grid cell can be considered to be divided into subregions containing distinct species. Then $\tilde{P}_i$, which is defined as $\tilde{P}_i = P_i/f_i$, is the pressure of the subregion containing species i. Since pressure remains continuous across surfaces, and each subregion of a cell can be assumed to be in pressure equilibrium with each other, then we have

$$\tilde{P}_i = P.$$

Thus, Eq. (22) becomes

$$\frac{1}{f_i}\frac{D}{Dt}(f_i) + \frac{1}{\gamma_i P}\frac{D}{Dt}(P) + \nabla\cdot\mathbf{u} = 0. \tag{23}$$

Summing the above equation over all species, with $\sum_{i=1}^{ns} f_i = 1$, leads to the following equation for the pressure of the mixture:

$$\frac{D}{Dt}(P) + \frac{P^2}{\sum_{i=1}^{ns}\frac{P_i}{\gamma_i}}\nabla\cdot\mathbf{u} = 0. \tag{24}$$

We may now transform (18) by using (23) and (24) to obtain a differential equation expressing the species energy independent of f_i:

$$\frac{\partial \rho_i E_i}{\partial t} + \nabla\cdot(\rho_i E_i \mathbf{u}) + Y_i \mathbf{u}\cdot\nabla P + \frac{P_i P}{\gamma_i \sum_{i=1}^{ns}\frac{P_i}{\gamma_i}}\nabla\cdot\mathbf{u} = 0. \tag{25}$$

For a single fluid, this equation becomes (14). Thus, for an ns-component gas mixture, the set of equations that needs to be discretized are (12) through (14), and (15) and (25) for $1 \le i \le (ns - 1)$. This comprises $(2ns + d)$ number of differential equations where d is the number of space dimensions.

In the next section, when we present the implementation of this equation into high-order schemes, characteristic variables (defined in the next section) are needed. Thus, we derive the Jacobian matrices and their eigenvalues and eigenvectors for the latter use. For the derivation, derivatives of pressure with respect to the flow variables are needed; thus, derivatives of γ are also involved. This would make the matrices very complicated. To circumvent this, we include the pressure equation in the system. The augmented system, in two dimensions, can be written as

$$\mathbf{V}_t + \mathbf{A}\mathbf{V}_x + \mathbf{B}\mathbf{V}_y = 0, \tag{26}$$

TABLE I

Matrix **L** (Right Eigenvectors of Jacobian Matrix **M**)

1	1	0	0	0	...	0	0	...	0	1
$u - k_1\hat{c}$	u	k_2	0	0	...	0	0	...	0	$u + k_1\hat{c}$
$v - k_2\hat{c}$	v	$-k_1$	0	0	...	0	0	...	0	$v + k_2\hat{c}$
$H - \hat{u}\hat{c}$	$\frac{u^2+v^2}{2}$	$\hat{v}$	1	0	...	0	0	...	0	$H + \hat{u}\hat{c}$
Y_1	Y_1	0	0	1	...	0	0	...	0	Y_1
...	...	...	...	...	...	...	...	...	...	...
Y_{ns-1}	Y_{ns-1}	0	0	0	...	1	0	...	0	Y_{ns-1}
$\hat{H}_1 - Y_1\hat{u}\hat{c}$	0	0	0	0	...	0	1	...	0	$\hat{H}_1 + Y_1\hat{u}\hat{c}$
...	...	...	...	...	...	...	...	...	...	...
$\hat{H}_{ns-1} - Y_{ns-1}\hat{u}\hat{c}$	0	0	0	0	...	0	0	...	1	$\hat{H}_{ns-1} + Y_{ns-1}\hat{u}\hat{c}$
$\hat{c}^2$	0	0	0	0	...	0	0	...	0	$\hat{c}^2$

where the vector **V** represents

$$\mathbf{V} = (\rho, \rho u, \rho v, \rho E, \rho Y_1, ..., \rho Y_{ns-1}, \rho_1 E_1, ..., \rho_{ns-1} E_{ns-1}, P)^T. \tag{27}$$

Since both **A** and **B** are of the form of a generic matrix **M** defined by

$$\mathbf{M} = \alpha\mathbf{A} + \beta\mathbf{B},$$

it is convenient to describe the eigenvalues and eigenvectors in terms of α and β. The eigenvalues for **M** are found to be

$$\begin{aligned} \lambda^{(1)} &= (\alpha u + \beta v) - \hat{c}\sqrt{\alpha^2 + \beta^2} \\ \lambda^{(2)} &= \cdots = \lambda^{(2ns+2)} = (\alpha u + \beta v) \\ \lambda^{(2ns+3)} &= (\alpha u + \beta v) + \hat{c}\sqrt{\alpha^2 + \beta^2}, \end{aligned} \tag{28}$$

with the effective speed of sound defined as

$$\hat{c} = \frac{P}{\sqrt{\rho \sum_{i=1}^{ns} (P_i/\gamma_i)}}. \tag{29}$$

Table I presents the matrix **L** which has the jth column as the right eigenvector $\mathbf{r}^{(j)}$ of **M**. The $\mathbf{L}^{-1}$ is given in Table II where the jth row of $\mathbf{L}^{-1}$ is the left eigenvector $\mathbf{l}^{(j)}$. The following nomenclature is used in the tables:

$$k_1 = \frac{\alpha}{\sqrt{\alpha^2 + \beta^2}}, \qquad k_2 = \frac{\beta}{\sqrt{\alpha^2 + \beta^2}}, \qquad H = E + \frac{P}{\rho},$$

$$\hat{H}_i = \frac{\rho_i E_i}{\rho} + \frac{P_i \hat{c}^2}{\gamma_i P}, \qquad \hat{u} = k_1 u + k_2 v, \qquad \hat{v} = k_2 u - k_1 v.$$

The eigenvalues are real and the eigenvectors are independent; hence, the degenerated system is still hyperbolic.

4. NUMERICAL METHOD

Equations (12)–(15) form a well known system of hyperbolic equations, written in conservative form. Without the chemical source term, it can be accurately simulated by many well developed schemes. The remainder of the equations, (25), is given in a non-conservative form. A numerical implementation of this equation into existing conservative, shock-capturing schemes, in particular the Godunov-type method, is provided in this section. For the proper treatment of the chemical source term, a splitting method with an enforcement of the reaction temperature is also presented. The resulting scheme conserves mass, momentum, and energy of the mixture. The scheme also is numerically and thermodynamically consistent. The description of the numerical method is presented in the following.

Let $\mathbf{U}_j$ represent a vector of $(2ns + d)$ components containing the conservative variables for cell j. In two dimensions the vector takes the form:

$$\mathbf{U} = (\rho, \rho u, \rho v, \rho E, \rho Y_1, ..., \rho Y_{ns-1}, \rho_1 E_1, ..., \rho_{ns-1} E_{ns-1})^T.$$

We denote $\mathbf{U}^-_{j+1/2}$ and $\mathbf{U}^+_{j+1/2}$ as the states of the fluid just to the left and right of the cell interface $j + \frac{1}{2}$ respectively. For first-order solutions, **U** is considered as piecewise constant over each cell. For higher order solutions, a reconstruction procedure is performed for each cell in order to generate higher order spatial approximations. In this study, we use the ENO reconstruction technique from [12]; in addition, we also make a modification to this scheme to prevent oscillations resulting from high order polynomials which interpolate across multiple discontinuities. In regions away from extreme points, the modification ensures that the values of interpolating polynomials at cell interfaces will be bounded by the cell average values on each side of the interface. The details will be presented elsewhere. Hence, for high order solutions, we apply the reconstruction to characteristic variables from the system of

TABLE II

Matrix $\mathbf{L}^{-1}$ (Left Eigenvectors of Jacobian Matrix $\mathbf{M}$)

$\frac{\hat{u}}{2\hat{c}}$	$-\frac{k_1}{2\hat{c}}$	$-\frac{k_1}{2\hat{c}}$	0	0	...	0	0	...	0	$\frac{1}{2\hat{c}^2}$
1	0	0	0	0	...	0	0	...	0	$\frac{-1}{\hat{c}^2}$
$-\hat{v}$	k_2	$-k_1$	0	0	...	0	0	...	0	0
$\frac{u^2+v^2}{2}$	$-u$	$-v$	1	0	...	0	0	...	0	$\frac{u^2+v^2}{2\hat{c}^2}-\frac{H}{\hat{c}^2}$
$-Y_1$	0	0	0	1	...	0	0	...	0	0
...	...	...	...	...	...	...	...	...	...	...
$-Y_{ns-1}$	0	0	0	0	...	1	0	...	0	0
$Y_1\hat{u}_2$	$-Y_1\hat{u}k_1$	$-Y_1\hat{u}k_2$	0	0	...	0	1	...	0	$-\frac{\hat{H}_1}{\hat{c}^2}$
...	...	...	...	...	...	...	...	...	...	...
$Y_{ns-1}\hat{u}^2$	$-Y_{ns-1}\hat{u}k_1$	$-Y_{ns-1}\hat{u}k_2$	0	0	...	0	0	...	1	$-\frac{\hat{H}_{ns-1}}{\hat{c}^2}$
$-\frac{\hat{u}}{2\hat{c}}$	$\frac{k_1}{2\hat{c}}$	$\frac{k_2}{2\hat{c}}$	0	0	...	0	0	...	0	$\frac{1}{2\hat{c}^2}$

equations in (26). As noted in the previous section, we use the vector $\mathbf{V}$ (Eq. (27)) instead of $\mathbf{U}$ for simplifying the derivation of the Jacobian matrices. The characteristic variables of $\mathbf{V}$ are defined as

$$w^{(k)} = \mathbf{l}^{(k)}\mathbf{V} \qquad k = 1, ..., 2ns + 3,$$

where $\mathbf{l}^{(k)}$ is the left eigenvector of $\mathbf{M}$ associated with $\lambda^{(k)}$. Then, the physical values can be obtained from the transformation

$$\mathbf{V} = \sum_{k=1}^{2ns+3} w^{(k)}\mathbf{r}^{(k)},$$

where $\mathbf{r}(^k)$ is the right eigenvector. We perform this reconstruction procedure in each spatial direction separately. The eigenvectors are evaluated at the cell in which the reconstruction is performed. Once the values of $\mathbf{U}^-$ and $\mathbf{U}^+$ are obtained to the desired order of accuracy, the state of the fluid at each cell interface, $\mathbf{U}^*$, is determined from the solution to the Riemann problem composed of left and right states, $\mathbf{U}^-$ and $\mathbf{U}^+$. The original Godunov method [10] is based on the exact solution of the Riemann problem; however, approximate Riemann solvers are often used in practice. We use the approach given in [5] in this paper. We emphasize here that the Riemann problem only needs to be solved *once* for the *mixture* of the fluid at each cell interface; species properties are then derived from the direction of propagation of the contact discontinuity. The procedure is given in the following.

Given $\mathbf{U}^-$ and $\mathbf{U}+$, a Riemann solver yields the mixture density ρ^*, pressure P^*, and normal velocity u_n^* at the cell interface. The species mass fractions are determined by the approach given in [17] as

$$Y_i^* = \begin{cases} Y_i^- & \text{if } u_n^* > 0 \\ Y_i^+ & \text{otherwise;} \end{cases} \tag{30}$$

it was shown in [17] that this condition would preserve the positivity of the mass fractions. Similarly, the tangential velocity is determined by

$$u_t^* = u_t^- \qquad \text{if } u_n^* > 0,$$

$$u_t^* = u_t^+ \qquad \text{otherwise.}$$

Since from the pressure equilibrium condition we have

$$f_i^- = \frac{P_i^-}{P^-}, \qquad f_i^+ = \frac{P_i^+}{P^+}, \qquad P_i = f_i P,$$

the partial pressure for species i can be obtained by

$$P_i^* = \begin{cases} \dfrac{P_i^- P^*}{P^-} & \text{if } u_n^* > 0 \\ \dfrac{P_i^+ P^*}{P^+} & \text{otherwise.} \end{cases} \tag{31}$$

The temperature for each species i is calculated from the ideal gas law as

$$T_i^* = \frac{P_i^* W_i}{\rho^* Y_i^* R_u}.$$

Then γ_i^* is calculated at $T = T_i^*$. The energy for each species i at the cell interfaces is calculated from (4) and the mixture energy is the summation of all species energy.

Next, we describe the procedure to advance the solution in time. We first consider the no-reaction case. The equations for the first $(ns + 1 + d)$ components of $\mathbf{U}$, i.e., (12)–(15) with $\dot{\omega}_i = 0$, in two dimensions can be written as:

$$\mathbf{U}_t^{(k)} + \mathbf{F}^{(k)}(\mathbf{U})_x + \mathbf{G}^{(k)}(\mathbf{U})_y = 0 \qquad k = 1, ..., (ns + 1 + d). \tag{32}$$

The semi-discrete form of the Godunov-type method is

$$\frac{\partial \overline{\mathbf{U}}_{i,j}^{(k)}}{\partial t} = -\frac{1}{\Delta x_{i,j}}[\mathbf{F}^{(k)}(\mathbf{U}^*(x_{i+1/2,j}, t)) - \mathbf{F}^{(k)}(\mathbf{U}^*(x_{i-1/2,j}, t))] - \frac{1}{\Delta y_{i,j}}[\mathbf{G}^{(k)}(\mathbf{U}^*(y_{i,j+1/2}, t)) - \mathbf{G}^{(k)}(\mathbf{U}^*(y_{i,j-1/2}, t))] \qquad k = 1, ..., (ns + 1 + d), \tag{33}$$

where $\overline{\mathbf{U}}$ is the cell average of $\mathbf{U}$. The remaining components of $\mathbf{U}$ are the energies of each species i for $1 \le i \le (ns - 1)$. They are given by (25) in a nonconservative form. In order to discretize this equation, we first examine the semidiscrete form of the mixture energy equation. Following (33) and restricting our attention to the x-direction, the semidiscrete form for (14) is written as

$$\frac{\partial \overline{(\rho E)}_{i,j}}{\partial t} = -\frac{1}{\Delta x_{i,j}}[\Delta(\rho E u) + \overline{u}\,\Delta P + \overline{P}\,\Delta u], \tag{34}$$

where $\Delta a = a_{i+1/2,j} - a_{i-1/2,j}$ and

$$\overline{a} = \frac{a_{i+1/2,j} + a_{i-1/2,j}}{2}.$$

We also have

$$\Delta(ab) = \overline{a}\,\Delta b + \overline{b}\,\Delta a.$$

Thus, Eq. (25) is discretized as

$$\frac{\partial \overline{\mathbf{U}}_{i,j}^{(k)}}{\partial t} = -\frac{1}{\Delta x_{i,j}}\left[\Delta(\rho_i E_i u) + \overline{Y}_i \overline{u}\,\Delta P + \overline{\left(\frac{P_i}{\gamma_i \sum_{i=1}^{ns} \frac{P_i}{\gamma_i}}\right)}\,\overline{P}\,\Delta u\right]^x - \frac{1}{\Delta y_{i,j}}\left[\Delta(\rho_i E_i v) + \overline{Y}_i \overline{v}\,\Delta P + \overline{\left(\frac{P_i}{\gamma_i \sum_{i=1}^{ns} \frac{P_i}{\gamma_i}}\right)}\,\overline{P}\,\Delta v\right]^y, \qquad k = (ns + 2 + d), ..., (2ns + d), \tag{35}$$

where $[\ ]^x$ and $[\ ]^y$ denote that operators perform respectively in the x- and y-directions, and the single subscript i refers to the ith species. This discretization is consistent in the sense that it reduces to (34) for a single fluid; hence, the overall method is consistent. We emphasize here that information from (35) is only used to obtain the mixture ratio of specific heats. Even though (35) is not in conservative form, the overall scheme can be considered conservative since it conserves the mixture mass, momentum, and energy, as well as the mass for each component.

The time discretization for (33) and (35) can be performed using the forward Euler equation if only first-order accurate solutions are desired. A Lax–Wendroff-type time discretization based on the Taylor series expansion for the conservative variables can be used to obtain second-order accurate solutions. First we calculate the values of $\mathbf{U}^-$ and $\mathbf{U}^+$ at time $t_{n+1/2}$ as

$$\mathbf{U}^{\pm}(t_{n+1/2}) = \mathbf{U}^{\pm}(t_n) - \frac{\Delta t}{2}\left[\mathbf{A}\frac{\partial \mathbf{U}}{\partial x} + \mathbf{B}\frac{\partial \mathbf{U}}{\partial y}\right]^{\pm},$$

where all the values on the right-hand side are obtained from the high-order (two or higher) reconstruction step; thus, the spatial accuracy is not restricted to second order. The Riemann solvers are then performed. For even higher orders of temporal accuracy, the method of lines is recommended, especially for multidimensional systems of equations.

For multidimensions, the reconstruction procedure is applied to each spatial direction separately while keeping all other variables fixed. Thus, the method in multidimensions is at most second order accurate in space. For higher orders of spatial accuracy in multidimensions, methods in [4] and [24] can be used.

For chemically reacting flows, we use splitting methods in which the chemistry is separated from the fluid motion, thus freeing the fluid terms from the restricted time scale imposed by the chemical reactions. The first fractional step solves the nonreactive flows by using the method presented above. The chemistry is then solved in the second step. Conservation of total mass implies

$$\frac{dY_i}{dt} = \frac{\dot{\omega}_i}{\rho} \qquad for\ i = 1, ..., ns, \tag{36}$$

where the right-hand side depends on species mass frac-

tions as well as on temperature. In addition, the total internal energy does not change. From the expression of specific internal energy for ideal gases

$$e = \sum_{i=1}^{ns} Y_i h_i - R_u \sum_{i=1}^{ns} \left(\frac{Y_i T_i}{W_i} \right),$$

we differentiate with respect to time with e being a constant. After substituting

$$\frac{dh_i}{dt} = c_{p,i} \frac{dT_i}{dt}$$

and using (36), we then have

$$\rho \sum_{i=1}^{ns} \left(c_{p,i} - \frac{R_u}{W_i} \right) Y_i \frac{dT_i}{dt} = \sum_{i=1}^{ns} \left(\frac{T_i R_u}{W_i} - h_i \right) \dot{\omega}_i.$$

For the reaction purposes, it is presumed that within a grid cell all species coexist at the same temperature. Then the equation for the mixture temperature is

$$\frac{dT}{dt} = \frac{\sum_{i=1}^{ns} \left(\frac{TR_u}{W_i} - h_i \right) \dot{\omega}_i}{\rho \sum_{i=1}^{ns} \left(c_{p,i} - \frac{R_u}{W_i} \right) Y_i}. \tag{37}$$

Hence, we update species mass fractions due to chemical reactions by integrating (36) and (37) from time $t = n$ to $t = n + \Delta t$. The energy for each species is then updated by using the new temperature and species mass fraction. Within each cell species energy can be created or destroyed due to chemical reactions, but the total energy is conserved. To obtain second order accuracy, either the Strang splitting [23] or the alternate switching of the fractional steps as shown in [6] can be implemented. For most applications, it is adequate to solve only (36) for Y_i using a fixed value of the mixture temperature determined from the first fractional step. But additional care must be taken when simulating stiff detonation waves.

To simulate stiff detonation waves, further restrictions on the burning rate must be applied in order to obtain correct physical results; an example is a fix presented by Engquist and Sjogreen in [9]. In the following we describe an alternative criterion. After the first fractional step, it is possible that both the flame and shock fronts are co-located within a large grid cell as shown in Fig. 3. During the second fractional step, only the unburnt gas region behind the shock can be burnt, consistent with the Zel'dovich, von Neumann, and Doring (ZND) model. But the *mixture* temperature for this cell can be high enough that both the post- and the pre-shock unburnt gas regions are completely burnt. This causes the shock to move at an incorrect speed. Hence, at the reaction front, the reaction temperature has to be the temperature of the post-shock unburnt gas. To enforce this criterion, we first locate the reaction front; its location is approximately at the position where the unburnt mass fraction, Y_u, is 0.5. Within each grid cell, the present scheme also provides the mixture temperature as well as the temperatures for each species. Thus, the reaction temperature is taken to be

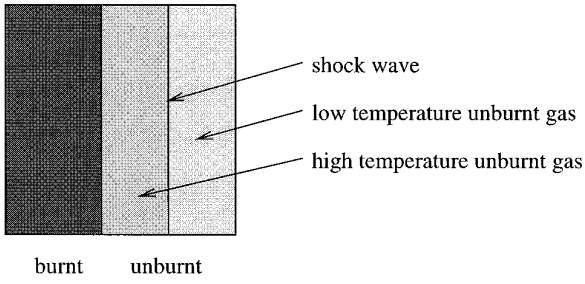

FIG. 3. Schematic of a subcell resolution for a fluid convection step.

$$T = \begin{cases} \tilde{T}_u & \text{if } Y_u \geq 0.5 \\ \tilde{T}_{\text{mixture}} & \text{otherwise,} \end{cases} \tag{38}$$

where $\tilde{T}_u$ and $\tilde{T}_{\text{mixture}}$ are obtained from the first fractional step.

5. NUMERICAL RESULTS

In this section we present results of several test problems in one and two space dimensions: a convection of a contact discontinuity, a shock tube with two species, a Chapman–Jouguet detonation wave, and an interaction of a shock wave with a cold helium cylinder. Solutions for first and higher order accurate methods are presented. We choose fourth order spatially accurate solutions as a representation of higher order solutions. The Lax–Wendroff–type time discretization is used; hence, second order temporal accuracy is obtained. In most of the following figures, we use plus (+) symbols to represent numerical solutions obtained from the thermodynamically consistent method presented here; solid lines are exact solutions. Comparisons with other methods are included. Solutions obtained from nu-

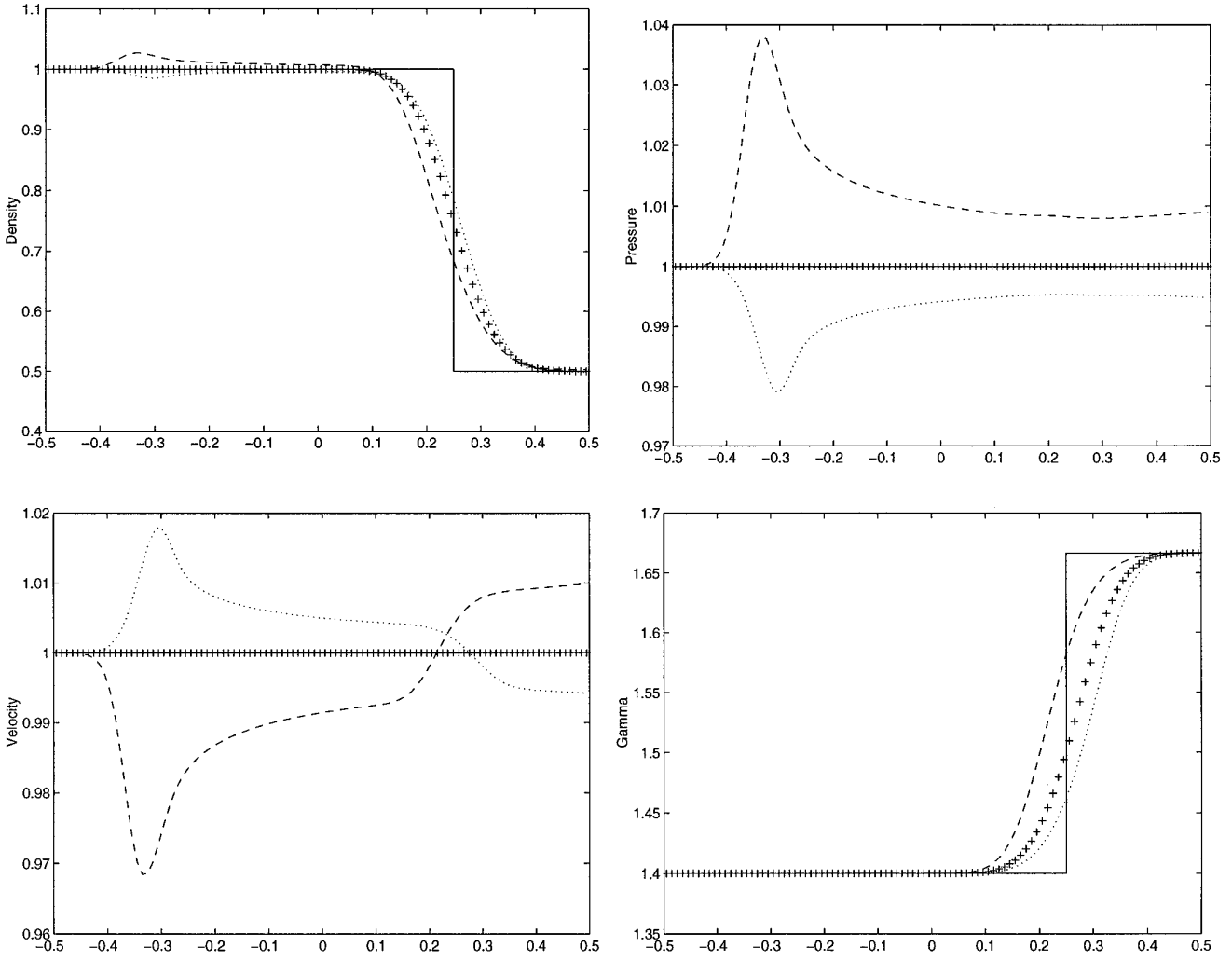

FIG. 4. Comparison of the thermodynamically consistent versus inconsistent numerical methods. Shown are first-order accurate solutions for the convection of a contact discontinuity at $t = 0.5$ with CFL = 0.8. (Solid lines, exact solutions; "+", consistent method; dashed lines, inconsistent method with γ calculated from Eq. (10); dotted lines, inconsistent method with γ calculated from Eq. (11).)

merical methods which solve the Euler equations written for the mixture and mass conservation equations for each species with γ calculated from (10) and (11) are presented as dashed and dotted lines respectively. These methods are referred to here as thermodynamically inconsistent methods, and the test problems are chosen so that the methods have difficulties in multispecies computations. All these simulations are computed from a two-dimensional code.

5.1. *Convection of a Contact Discontinuity*

We examine the convection of a contact discontinuity which separates air (species 1) and helium (species 2). The pressure and normal velocity are unity. The properties of the gases are given in the example presented in Section 2. The initial conditions (non-dimensionalized) are

$$\begin{aligned} (\rho, \gamma, Y_1, Y_2) &= (1, 1.4, 1, 0) \qquad && x < -0.25 \\ (\rho, \gamma, Y_1, Y_2) &= (0.5, 1.667, 0, 1) \qquad && x \geq -0.25, \end{aligned} \tag{39}$$

where x varies from -0.5 to 0.5. We use 100 cells in the calculations. Figure 4 shows a comparison of the results from the three different methods, as well as the exact solution, at time $t = 0.5$, with CFL = 0.8. For direct comparisons, first order accurate solutions are presented. The exact solution has a contact discontinuity at $x = 0.25$, and pressure and velocity remain exactly at unity. For the solutions obtained from the thermodynamically inconsistent

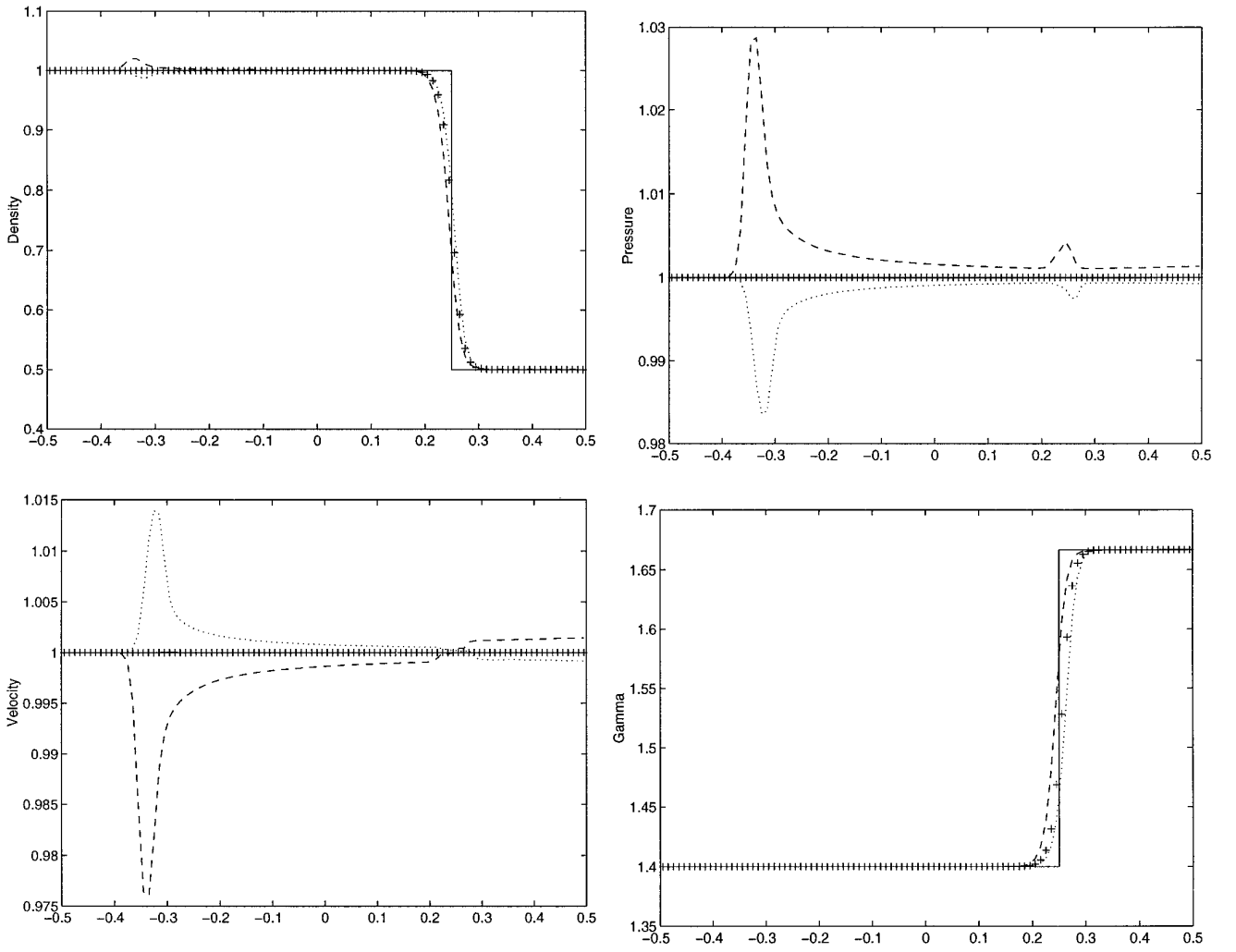

FIG. 5. Comparison of the thermodynamically consistent versus inconsistent numerical methods. Shown are fourth-order spatial with second-order temporal accurate solutions for the convection of a contact discontinuity at $t = 0.5$ with CFL = 0.8. (Solid lines, exact solutions; "+", consistent method; dashed lines, inconsistent method with γ calculated from Eq. (10); dotted lines, inconsistent method with γ calculated from Eq. (11).)

methods (dashed and dotted lines), there are over- and under-shoots in the pressure field with the peaks located near the initial location of the contact discontinuity. These numerical errors propagate throughout the region and also contaminate the density and velocity fields. There are also erroneous steps across the discontinuity in the velocity profiles. The speeds of the discontinuity are also under- and over-predicted, as can be seen from the density plot. For the consistent method, the results are in excellent agreement with the exact solution. The pressure and velocity remain in equilibrium. The speed of the contact discontinuity and the jump in density are correctly predicted. Since γ is not a conserved property, it is not expected to be symmetric about the discontinuity. Other models for γ give over- and under-estimated values. The computational time for the consistent method is 15% higher than that of the inconsistent methods.

Solutions computed by the fourth order accurate in space and second order accurate in time method are presented in Fig. 5. The discontinuity is better resolved. Even though the solutions show some improvement in resolving the magnitude of variables across the discontinuity, the numerical spikes resulting from using (10) or (11) still persist. High order accurate solutions of the consistent method encounter no numerical difficulty.

5.2. *Shock Tube with Two Species*

The next test problem is a shock tube, open at both ends, initially with a diaphragm separating air (species 1)

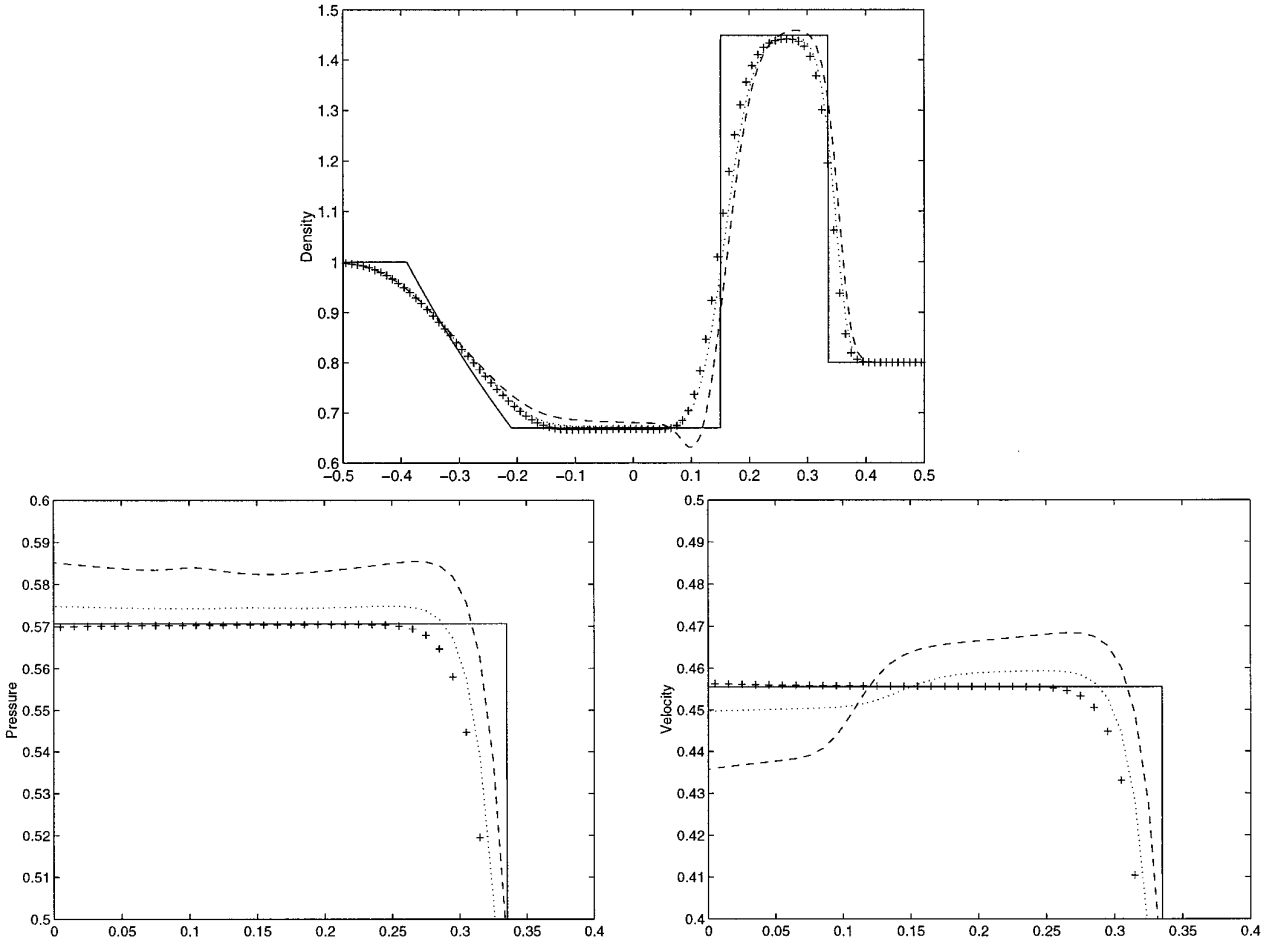

FIG. 6. Comparison of the thermodynamically consistent versus inconsistent numerical methods. Shown are first-order accurate solutions for the two species shock tube at $t = 0.33$ with CFL $= 0.8$ (solid lines, exact solutions; "+", consistent method; dashed lines, inconsistent method with γ calculated from Eq. (10); dotted lines, inconsistent method with γ calculated from Eq. (11)).

to the left and helium (species 2) to the right. The initial data (nondimensionalized) are

$$\begin{aligned}(\rho, P, u, \gamma, Y_1, Y_2) &= (1, 1, 0, 1.4, 1, 0) \qquad x < 0\\ (\rho, P, u, \gamma, Y_1, Y_2) &= (0.8, 0.2, 0, 1.667, 0, 1) \qquad x \geq 0,\end{aligned} \tag{40}$$

where x varies from -0.5 to 0.5. This set of initial data is chosen so that there is a large jump in temperature across the contact discontinuity after the passage of the shock wave. Thus, errors committed at the discontinuity can be easily visualized. We use 100 cells with a uniform spacing in the simulation. Figure 6 shows the comparisons of the results from the three different methods and the exact solution at time $t = 0.33$ with CFL $= 0.8$. The exact solution has a contact discontinuity and a shock at $x = 0.150$ and $x = 0.336$, respectively. First order accurate solutions are shown in the figure. It is clear that the inconsistent methods have difficulties resolving the contact discontinuity. There is an erroneous dip in the density profile across the contact discontinuity for the inconsistent method with γ calculated from (10). The pressure and velocity in the enlarged region of the contact discontinuity are shown in the figure. Across the contact discontinuity, i.e., $x = 0.15$, both of the inconsistent methods over-predict the pressure by 2% and 1%, respectively. There is also a nonphysical step in the velocity profile at the location of the contact discontinuity for these methods. The results from the consistent method show good agreement with the analytical solution.

Solutions computed by the fourth order accurate in space and second order accurate in time method are presented in Fig. 7. For each case the contact discontinuity is better resolved; the erroneous step in the velocity profile is improved. Even though the errors are smaller, they are not

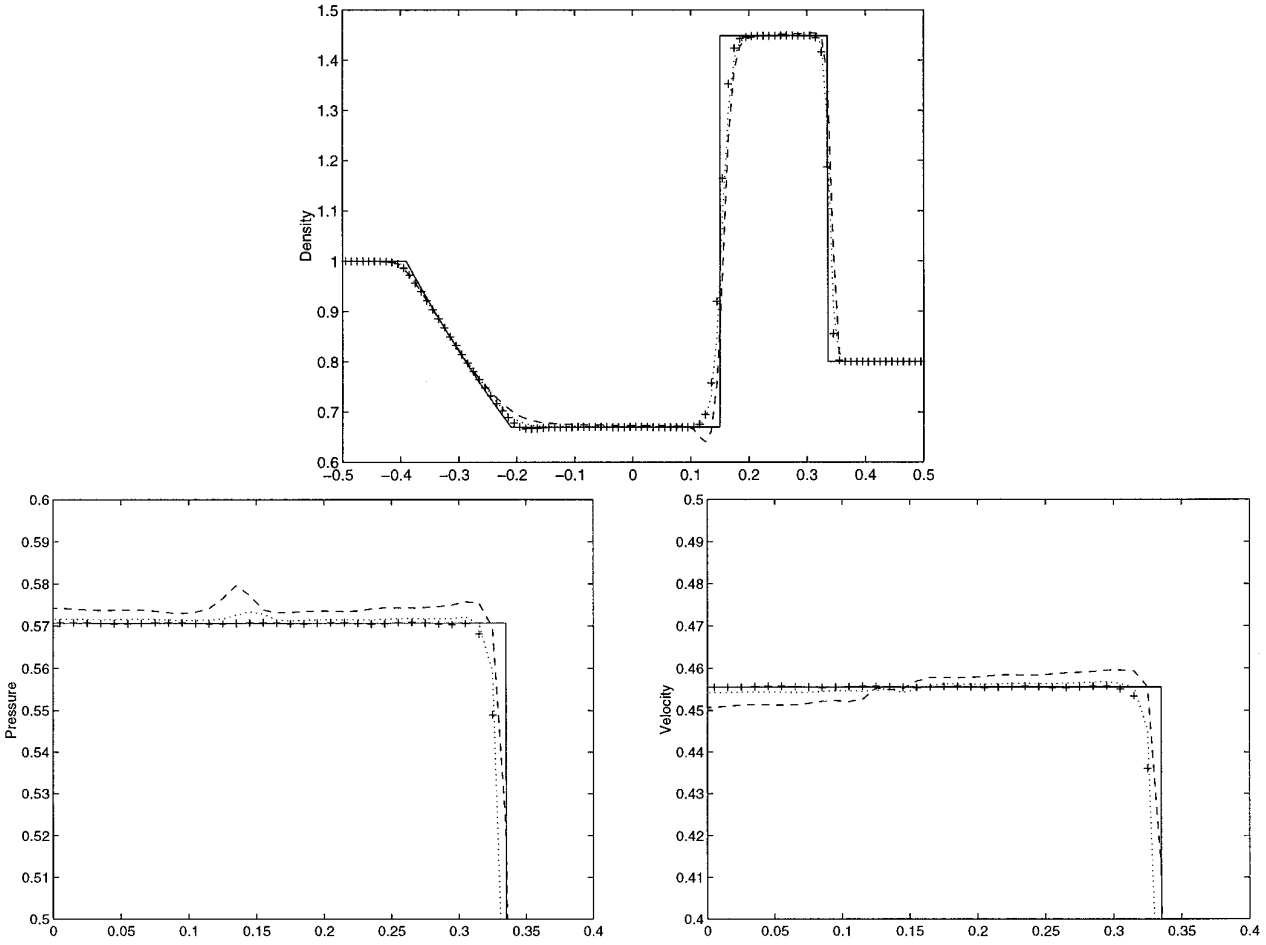

FIG. 7. Comparison of the thermodynamically consistent versus inconsistent numerical methods. Shown are fourth-order spatial with second-order temporal accurate solutions for the two species shock tube at $t = 0.33$ with CFL = 0.8 (solid lines, exact solutions; "+", consistent method; dashed lines, inconsistent method with γ calculated from Eq. (10); dotted lines, inconsistent method with γ calculated from Eq. (11)).

completely eliminated. The high order accurate solutions obtained from the consistent method show excellent agreement with the exact solution. The method has also been applied to test problems in [1, 15, and 17]. The results agree well with analytical solutions. These results are not shown here since they exhibit behavior similar to this test problem.

5.3. *Chapman–Jouguet Detonation Wave*

A stiff Chapman–Jouguet (C-J) detonation wave is simulated in this section. We simulate ozone decomposition; the data are taken from [6]. Both unburned (species 1) and burned (species 2) gases are perfect gases with a constant ratio of specific heats of 1.4. A one-step, irreversible reaction is assumed; a simplified Arrhenius model is used where the reaction rate is a step function depending on temperature. The mass production rate thus becomes

$$\dot{\omega}_1 = -K\rho Y_1 H(T - T_c),$$

where T_c is the critical temperature and the Heavyside function $H(T)$ takes the form

$$H(T) = \begin{cases} 1 & T > T_c \\ 0 & \text{otherwise.} \end{cases} \tag{41}$$

The constants are given as

$$T_c = 500\ \text{K}, \qquad K = 5.825 \times 10^9\ \text{sec}^{-1},$$
$$h^0_{f,1} = 5.196 \times 10^9\ \text{dynes–cm/g}.$$

For certain values of the wave propagation speed and activation energy, the flowfield can be unsteady where the

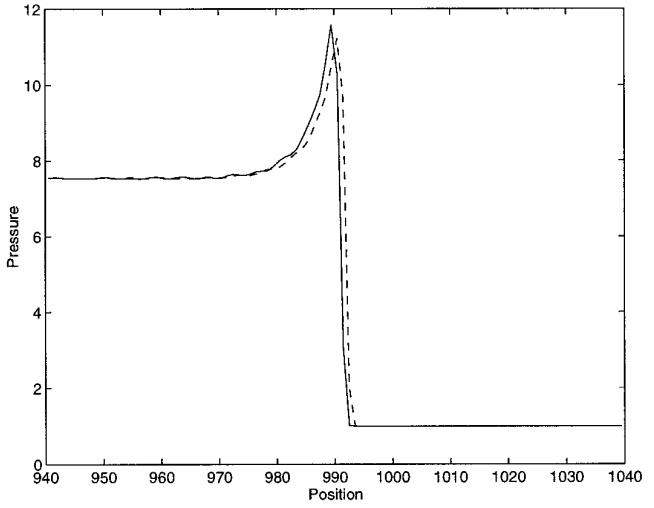

FIG. 8. Comparison of the splitting methods with and without the enforcement for the reaction temperature. Shown are solutions with a fine mesh for the Chapman–Jouguet detonation wave; $x_{\text{ref}} = 5 \times 10^{-6}$ cm, $t = 2.419 \times 10^2$, CFL = 0.8 (Solid lines, with the enforcement of Eq. (38); dashed lines, without (38).)

flow can be oscillating in a periodic or irregular manner. Through numerical experiments, the C-J deontation wave is found to be stable with the reaction rate defined as above.

The initial states for the unburned gas are

$$\rho = 1.201 \times 10^{-3}\ \text{g/cm}^3,$$
$$P = 8.321 \times 10^5\ \text{dynes/cm}^2, \qquad u = 0.$$

Here, we will express all variables in terms of some reference length x_{ref}, pressure P_{ref}, density ρ_{ref}, and molecular weight W_{ref}. Thus, specific energy, temperature, velocities, and time are normalized respectively by

$$E_{\text{ref}} = \frac{P_{\text{ref}}}{\rho_{\text{ref}}}, \qquad T_{\text{ref}} = \frac{P_{\text{ref}} W_{\text{ref}}}{\rho_{\text{ref}} R_u},$$
$$u_{\text{ref}} = \sqrt{\frac{P_{\text{ref}}}{\rho_{\text{ref}}}}, \qquad t_{\text{ref}} = \frac{x_{\text{ref}}}{\sqrt{\frac{P_{\text{ref}}}{\rho_{\text{ref}}}}}.$$

The reference pressure and density are taken to be the respective values of the unburned gas. The grid size is chosen as the reference length. The computed C-J initial states for the burned gas, in dimensionless form, are

$$\rho = 1.619, \qquad P = 7.535, \qquad u = 1.581,$$

and the normalized speed of the C-J detonation wave is 4.133.

The initial conditions have the C-J states defined for $x < 0$. We use 100 cells in all the simulations. To follow the moving wave, we allow the solution to run until the wave comes within a fixed distance from the center of the grid; then a fixed number of cells is added to the right while the same number of cells is eliminated at the left. First, we perform a simulation using an extremely fine mesh with $x_{\text{ref}} = 5 \times 10^{-6}$ cm. There are roughly 10 points in the reaction zone. Figure 8 displays the results for the pressure field at time $t = 2.419 \times 10^2$ with CFL = 0.8. The solid line repesents the solutions obtained from the splitting method with the enforcement of Eq. (38), while

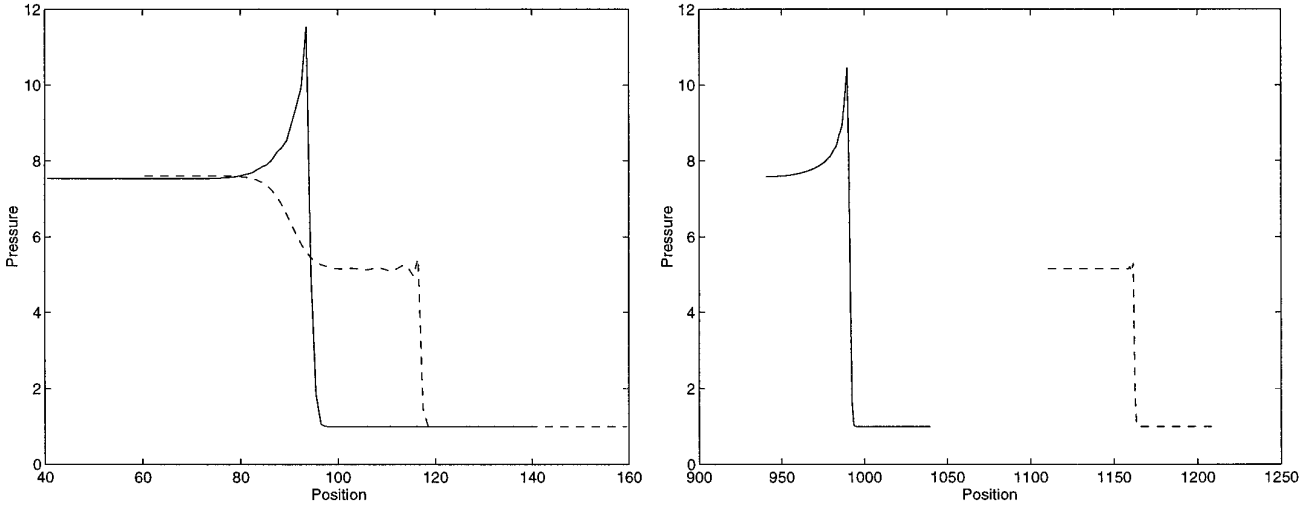

FIG. 9. Comparison of the splitting methods with and without the enforcement for the reaction temperature. Shown are solutions with a coarse mesh for the Chapman–Jouguet detonation wave; $x_{\text{ref}} = 5 \times 10^{-4}$ cm, $t = 24.193$ and 2.419×10^2 respectively, with CFL = 0.8 (solid lines, with the enforcement of Eq. (38); dashed lines, without (38)).

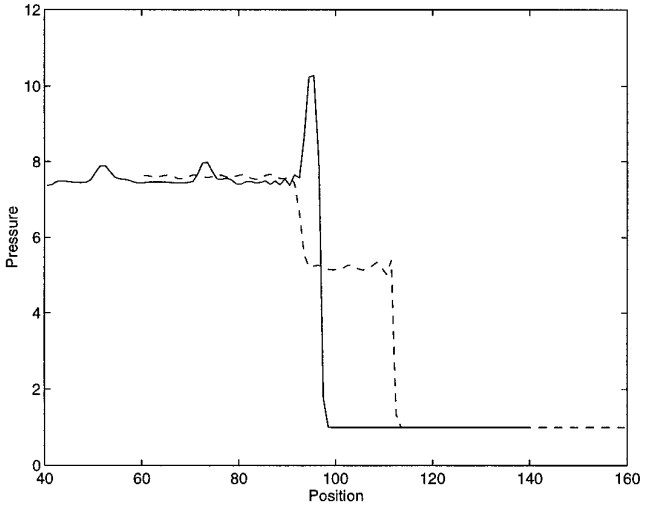

FIG. 10. Comparison of the splitting methods with and without the enforcement for the reaction temperature. Shown are high-order accurate solutions with a coarse mesh for the Chapman–Jouguet detonation wave; $x_{\text{ref}} = 5 \times 10^{-4}$ cm, $t = 24.193$, CFL = 0.8 (solid lines, with the enforcement of Eq. (38); dashed lines, without (38)).

the dashed line represents the solutions obtained without (38). The reaction zone with the ZND profile is correctly resolved by either method. The exact solution of the C-J wave has a shock front at $x = 1000$. Both methods slightly under-predict the location of the wave. This error is caused by the approximation of the initial wave without the ZND profile.

Next we increase the grid size by two orders of magnitude greater than those above, hence $x_{\text{ref}} = 5 \times 10^{-4}$ cm. The first order accurate solutions at time $t = 24.193$ and 2.419×10^2 are respectively shown in Fig. 9. The method without the enforcement of (38) gives nonphysical results; these are similar to the results obtained in [6]. The correct solutions of the detonation wave are obtained by the present method. Similar behavior is obtained for solutions computed by the fourth order accurate in space and second order accurate in time method; they are presented in Fig. 10.

5.4. *Interaction of a Shock Wave with a Cold Helium Cylinder*

Studies of the transmission and reflection of a weak shock wave from cylindrical and spherical gas inhomogeneities were investigated experimentally in [22] and later in [11]. The latter experiment has been simulated in [21]. The concept of shock-induced enhancement of mixing was first proposed in [19] for its potential application to scramjet combustor design. This concept is based on the high degree of vorticity generation that can arise when a shock wave interacts with an interface separating lighter gas from heavier gas. Experiments in [13] verified mixing enhancement in this problem. Numerical studies for the mixing enhancement problem have been performed in [8, 26, and 28]. In these studies, the embedded gas and its surrounding initially have the same temperature; whereas, for realistic engineering applications, the gas inhomogeneities usually have temperature different from the surroundings. A typical example is the injection of fuel jets into a hot stream. Thus, our objectives in this section are: (1) to show that numerical difficulties can arise in resolving material interfaces in realistic flow environments and (2) to demonstrate the accuracy of the current approach in simulating such flows.

We examine the interaction of a shock wave with a cold helium cylinder. Initially the helium region and the surrounding air have the same pressure, but the temperature of the helium region is equal to half of the surrounding air temperature. This cylindrical region has a unit radius, and its center is located at $x = 2$. An incident shock wave, initially located at $x = 0.5$, travels from left to right at Mach 1.093. The computational domain is a rectangular region with a uniform grid of 100×50 cells; the grid spacing is $\Delta x = \Delta y = 0.05$. To represent initially a cylinder on a Cartesian grid, for cells that contain the boundary of the cylinder, we interpolate the conservative values based on the cell volume fraction. While a second order accurate scheme is applied to time evolution, a fourth order accurate reconstruction procedure is used in each spatial direction. This is done to obtain a high resolution solution, even though the formal accuracy of the method is second order. To further achieve higher resolution at the material interfaces, the local adaptive mesh refinement technique in [3] is employed. Two levels of grids with a refinement factor of four are used. The lower half-plane is symmetric with respect to the upper half-plane, hence only the upper half of the system is simulated. The bottom boundary condition is the line of symmetry. At other boundaries, all gradients are set to zero to allow waves to propagate naturally out of the computational domain.

Figure 11 displays contour plots for the air mass fractions. Solutions obtained by the thermodynamically consistent and inconsistent methods are shown at time $t = 7.5$. At this time, the shock has already propagated out of the computational domain. As the incident shock passes through at earlier times, it deposits vorticity on the jet interface at a rate proportional to $(\nabla p \times \nabla \rho)$. Hence, the vorticity has a counterclockwise direction for the upper half-plane. This causes the upstream air to turn downward and form a high velocity re-entrant airstream along the centerline. As time passes, the upstream face of the cylinder continues to deform into a kidney-shaped structure. The consistent method encounters no difficulty in resolving the interface. For the inconsistent method, there are kinks generated by numerical errors along the interface; thus it is

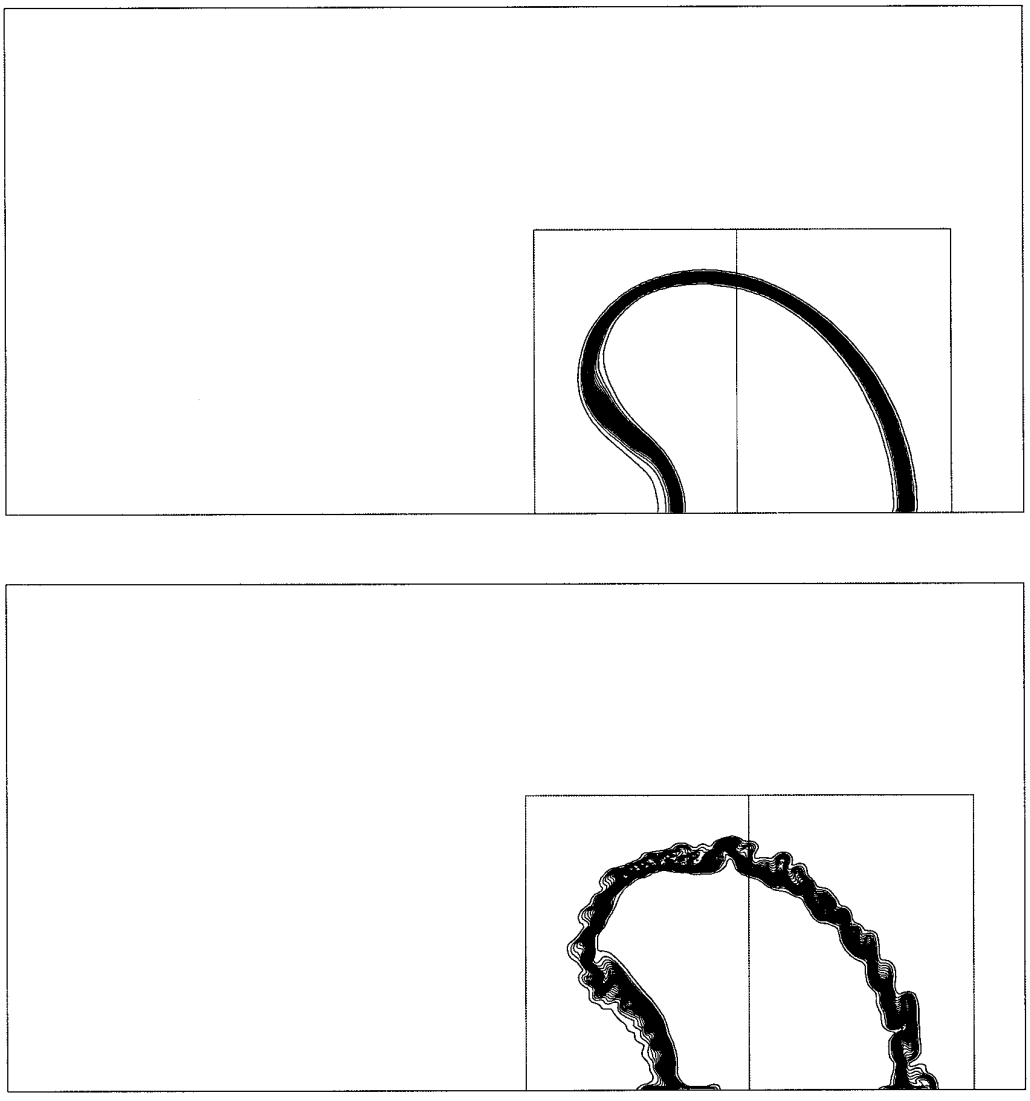

FIG. 11. Comparison of the thermodynamically consistent versus inconsistent numerical methods. Shown are 30 equally spaced contour lines for the mass fraction of the interaction of a Mach 1.093 shock wave with a cold helium cylinder embedded in air at $t = 7.5$.

clear that the inconsistent method has difficulties resolving contact surfaces separating gases with different ratios of specific heats and temperature.

6. SUMMARY

The imporance of enforcing thermodynamic consistency for the accurate solutions of nonequilibrium flows is demonstrated. The consistent formulation requires an additional set of species energy equations. An implementation of this consistency into existing conservative shock-capturing schemes is presented. For a two-dimensional code simulating two-species flows, solving the additional equation requires 15% more computing time. In solving chemically reacting flows, an enforcement of the reaction temperature that depends on the temperatures of each species is introduced to eliminate the nonphysical waves generated by stiff reaction fronts.

ACKNOWLEDGMENTS

I particularly like to acknowledge the guidance and encouragement from Marsha Berger, my mentor at the Courant Institute. She provided the adaptive mesh refinement code used in the example of the interaction of a shock wave with a cold helium cylinder. I would also like to thank Jonathan Goodman for many stimulating discussions. Thanks are also due to Smadar Karni, Michael Minion, and David Muraki for their constructive comments. This work was performed under the auspices of the

U.S. Department of Energy Contract DE-FG02-88ER25053 and DE-FG02-92ER25139.

REFERENCES

1. R. Abgrall, *Recherche Aerospatiale* **6** (1988).
2. J. Bell, M. J. Berger, J. Saltzman, and M. Welcome, *SIAM J. Sci. Comput.* **15,** 127 (1994).
3. M. J. Berger and P. Colella, *J. Comp. Phys.* **84,** 64 (1989).
4. J. Casper, AIAA Paper No. 91-0631, 1991 (unpublished).
5. P. Colella, *SIAM J. Sci. Statist. Comput.* **3,** 76 (1982).
6. P. Colella, A. Majda, and V. Roytburd, *SIAM J. Sci. Statist. Comput.* **7,** 1059 (1986).
7. P. Colella, H. M. Glaz, and R. E. Ferguson, ''Multifluid Algorithms for Eulerian Finite Difference Methods,'' paper to appear.
8. J. P. Drummond, AIAA Paper No. 91-1914, 1991 (unpublished).
9. B. E. Engquist and B. Sjogreen, UCLA CAM Report 91-03, 1991 (unpublished).
10. S. K. Godunov, *Mat. Sb.* **47,** 271 (1959) (Russian).
11. J.-F. Hass and B. Sturtevant, *J. Fluid Mech.* **181,** 41 (1987).
12. A. Harten, B. E. Engquist, S. J. Osher, and S. Chakravarthy, *J. Comp. Phys.* **71,** 231 (1987).
13. J. W. Jacobs, *J. Fluid Mech.* **234,** 629 (1992).
14. S. Karni, *J. Comp. Phys.* **112,** 31 (1994).
15. S. Karni, ''Hybrid Multifluid Algorithms,'' to appear.
16. B. Larrouturou and L. Fezoui, *Non-linear Hyperbolic Problems,* edited by Carasso, Charrier, Hanouzet, and Joly, Lecture Notes in Mathematics, Vol. 1402, (Springer-Verlag, New York/Berlin, 1988).
17. B. Larrouturou, *J. Comp. Phys.* **95,** 59 (1991).
18. R. J. LeVeque and H. C. Yee, *J. Comput. Phys.* **86,** 187 (1990).
19. F. E. Marble, G. J. Hendricks, and E. E. Zukoski, *Turbulent Reactive Flow,* R. Borghi and S. N. B. Murphy, Lecture Notes in Engineering, Vol. 40 (Springer-Verlag, New York/Berlin, 1989), p. 932.
20. E. S. Oran, T. R. Young, and J. P. Boris, *Combustion and Flame* **48,** 135 (1982).
21. J. M. Picone and J. P. Boris, *J. Fluid Mech.* **189,** 23 (1988).
22. G. Rudinger and L. M. Somers, *J. Fluid Mech.* **7,** 161 (1960).
23. G. Strang, *SIAM J. Numer. Anal.* **5,** 506 (1968).
24. C. W. Shu and S. J. Osher, *J. Comput. Phys.* **83,** 32 (1989).
25. V. T. Ton, A. R. Karagozian, B. E. Engquist, and S. J. Osher, *Western States Section/the Combustion Institute,* 1991 Fall meeting, Paper 91-101, 1991 (unpublished).
26. V. T. Ton, A. R. Karagozian, F. E. Marble, S. J. Osher, and B. E. Engquist, *Theoret. Comput. Fluid Dynamics* **6,** 161 (1994).
27. F. A. Williams, *Combustion Theory* (Addison-Wesley, Reading, MA, 1985).
28. J. Yang, Ph.D. thesis, California Institute of Technology, 1991.